Split-Channel Ballistic Transport in an InSb Nanowire

Juan Carlos Estrada Saldaña,[†,∇] Yann-Michel Niquet,[§] Jean-Pierre Cleuziou,[†] Eduardo J. H. Lee,[†,○] Diana Car,[⊥] Sébastien R. Plissard,[#] Erik P. A. M. Bakkers,[⊥] and Silvano De Franceschi*[,†]
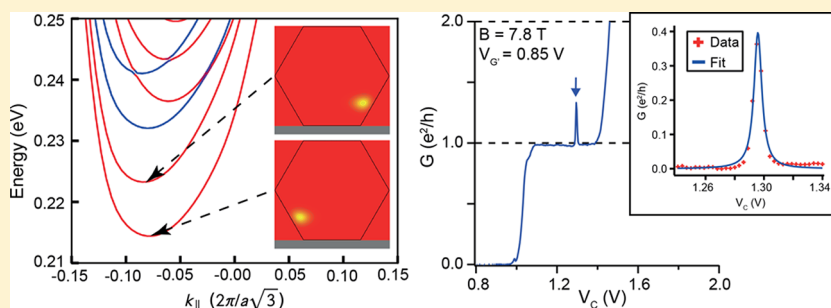
[†]University Grenoble Alpes & CEA, INAC-PHELIQS, F-38000 Grenoble, France
[§]University Grenoble Alpes & CEA, INAC-MEM, F-38000 Grenoble, France
[⊥]Technische Universiteit Eindhoven, P.O. Box 513, 5600 MB Eindhoven, The Netherlands
[#]CNRS, LAAS-CNRS, Université de Toulouse, 31400 Toulouse, France

S Supporting Information

ABSTRACT: We report an experimental study of one-dimensional (1D) electronic transport in an InSb semiconducting nanowire. A total of three bottom gates are used to locally deplete the nanowire, creating a ballistic quantum point contact with only a few conducting channels. In a magnetic field, the Zeeman splitting of the corresponding 1D sub-bands is revealed by the emergence of conductance plateaus at multiples of e^2/h, yet we find a quantized conductance pattern largely dependent on the configuration of voltages applied to the bottom gates. In particular, we can make the first plateau disappear, leaving a first conductance step of $2e^2/h$, which is indicative of a remarkable 2-fold sub-band degeneracy that can persist up to several tesla. For certain gate voltage settings, we also observe the presence of discrete resonant states producing conductance features that can resemble those expected from the opening of a helical gap in the sub-band structure. We explain our experimental findings through the formation of two spatially separated 1D conduction channels.

KEYWORDS: Conductance quantization, one-dimensional transport, nanowire, band structure, helical liquid, Majorana fermions

One-dimensional (1D) nanowires made of small band gap semiconductors, such as InSb or InAs, have been identified as a promising material system for the realization of topological superconductivity.[1,2] This exotic state of matter, which is characterized by the emergence of zero-energy Majorana quasiparticles localized at the nanowire edges, is expected to occur only when some key requirements are simultaneously met.[3,4] Above all, the nanowire has to be 1D and at most moderately disordered.[5−7]

The linear conductance of a clean, ballistic 1D nanowire is expected to be quantized. At zero magnetic field, B, time-reversal symmetry leads to doubly degenerate sub-bands yielding conductance plateaus at multiples of $2e^2/h$, where e is the electron charge and h the Planck constant.[8] This 2-fold degeneracy gets lifted at finite B leading to e^2/h conductance steps.

While the low-temperature transport properties of semi-conductor nanowires have been studied for more than 15 years,[9] the achievement of ballistic 1D conduction has been challenging due to the presence of disorder of various origin.[10−15] Following some initial experimental signatures in Ge/Si core/shell nanowires,[16] further experimental evidence of conductance quantization was more recently reported using either InAs[17−23] or InSb nanowires.[24−27] In these studies, conductance plateaus were observed by sweeping the voltage of a single gate, creating a tunable electrostatic potential barrier in the nanowire. Here, we investigate conductance quantization in an InSb nanowire simultaneously gated by three closely spaced electrodes. This increased complexity results in an enhanced tunability of the local conduction-band profile, giving access to unexpected properties of the 1D electronic sub-bands.

The studied device, shown in Figure 1a, was fabricated from a 160 nm diameter InSb nanowire. In an optical setup equipped with a micromanipulator, the nanowire was picked from its growth substrate and deposited on a bed of bottom gates covered by 10 nm of hafnium oxide. Source and drain contacts were defined by e-beam lithography followed by Ar sputtering and in situ e-beam evaporation of 120 nm-thick Al. A total of

(a)   (b)
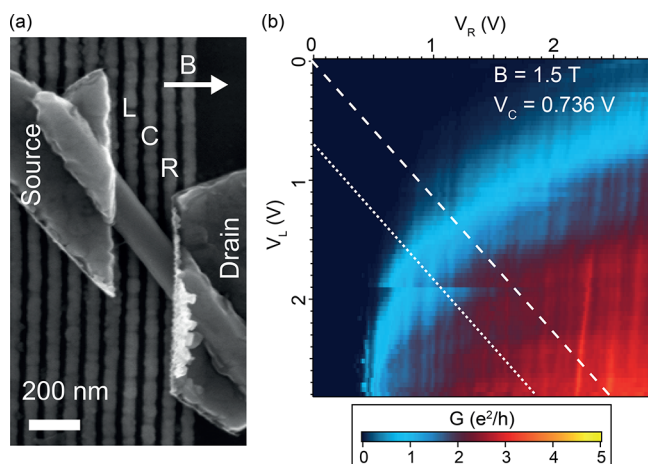
Figure 1. (a) Scanning electron micrograph of the device. The magnetic field was applied in the plane of the substrate and at an angle of 58° relative to the nanowire axis. (b) Linear conductance, G, as a function of the two lateral gate voltages, V_L and V_R, at a fixed voltage V_C on the central gate. The dotted (dashed) white line indicates the gate sweeping trajectory for the data in Figure 2 (Figure 4).

three local bottom gates, labeled as L (left), C (central), and R (right), were used to deplete the nanowire channel. Magneto-transport measurements were performed in a He-3 refrigerator with a base temperature of 260 mK.

Figure 1b shows a color plot of the linear conductance, G, as a function of voltages V_L and V_R applied to gates L and R, respectively. Gate C is simultaneously set to $V_C = 0.736$ V, and an in-plane magnetic field $B = 1.5$ T is applied, as indicated in Figure 1a. This measurement shows that V_L and V_R have a balanced effect with comparable capacitive couplings reflecting the nominally identical widths of the corresponding gates. In the following, we shall present data sets in which gates L and R are swept together, along diagonal trajectories in the (V_L, V_R) plane, as indicated by the white lines in Figure 1b. The underlying idea is that sweeping along these lines from top-left to bottom-right corresponds to changing the longitudinal potential landscape from a double-humped to a single-humped camel back shape. At the transition, the conduction band is expected to present a single, relatively long and approximately flat potential barrier whose height can be adjusted by varying V_C.

The first data set is shown in Figure 2, where gate voltages V_L and V_R are swept along the dotted line in Figure 1b. In our notation, each gate-voltage sweep is parametrized by V_G, such that $V_L = V_G$ and $V_R = \alpha_{R/L}(V_L - V_{L_0})$, with $V_{L_0} = 0.74$ V and $\alpha_{R/L} = 0.875$. A set of $G(V_C)$ traces taken at $B = 5$ T at four different values of V_G is displayed in Figure 2a. The traces show plateaus of quantized conductance at multiples of e^2/h. Remarkably, the gate width of the plateaus varies with V_G. In particular, the e^2/h and the $3e^2/h$ plateaus smoothly shrink as V_G is increased, whereas the $2e^2/h$ plateau simultaneously broadens. At such a high B, the large Zeeman splitting, E_Z, expected in InSb should lift the 2-fold sub-band degeneracy and give rise to a first conductance step of e^2/h, as indeed observed earlier.[24] Instead, at $V_G = 4$ V (blue trace) the first e^2/h plateau has completely vanished, leaving a $2e^2/h$ conductance step. This behavior would be compatible with the hypothesis of a lowest energy sub-band with largely suppressed g-factor, resulting in a quasi-2-fold degeneracy. In fact, we provide an alternative interpretation, as discussed further below.

(a)   (b)
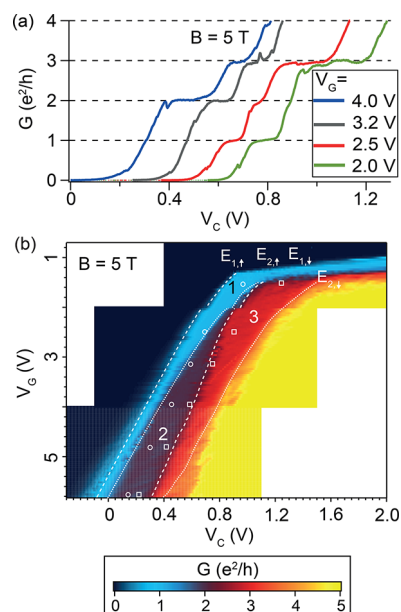
Figure 2. (a) Influence of V_G on the linear conductance $G(V_C)$ at $B = 5$ T. The e^2/h plateau is missing in the leftmost (blue) curve, and the $2e^2/h$ plateau has almost entirely vanished in the rightmost (green) curve. (b) Linear conductance maps at $B = 5$ T as a function of V_C and V_G. The bottom energies of the ↑ and ↓ spin components of the two first sub-bands are indicated by dashed (first sub-band) and dotted (second sub-band) lines. Open circles and squares indicate the barycenters of the two sub-bands, which provide a measure of the sub-band spacing ΔE.

A first intuition of the underlying scenario can be acquired from the two-dimensional color plot of $G(V_C, V_G)$ shown in Figure 2b. Here the color scale has been adjusted to emphasize the plateaus at e^2/h, $2e^2/h$, $3e^2/h$, and $4e^2/h$. Dashed (dotted) lines denote the conductance steps associated with the onset of conduction through the two pseudospin components, ↑ and ↓, of the first (second) spin-split sub-band. These lines correspond to aligning the spin-resolved sub-band edges with the Fermi energies of the leads (which coincide in the linear regime, i.e., for no DC bias-voltage between source and drain). We denote the energies of the sub-band edges as $E_{n,\uparrow}$ and $E_{n,\downarrow}$, where $n = 1$ or 2 is the orbital quantization number.

This assignment leads us to the following considerations. The two pseudospin components of the second sub-band exhibit an almost V_G-independent spacing, which may suggest a roughly constant Zeeman splitting. This is not the case for the first sub-band though. In fact, the relationship between V_C spacing and Zeeman splitting is not so straightforward. From a careful analysis of finite-bias measurements (i.e., differential conductance as a function of source-drain bias voltage, V_{sd}, and V_C), we find that the observed V_G dependence of the sub-band splittings originates mostly from variations in the lever-arm parameter relating V_C to sub-band energy. This analysis is presented in the Supporting Information. Interestingly, it reveals that the two spin-split sub-bands have significantly distinct lever arm parameters, denoting different capacitive couplings to gate C. Upon increasing V_G from 2 to 4 V, the lever-arm parameter of the first spin-split sub-band, α_1, varies from 0.062 ± 0.010 to 0.037 ± 0.008 eV/V. The one for the second spin-split sub-band, α_2, is less affected by V_G, varying from 0.040 ± 0.006 to 0.029 ± 0.005 eV/V, the variation occurring mainly between $V_G = 2$ and 2.5 V. Within the

experimental uncertainty, the two spin-split sub-bands exhibit the same Zeeman energies and, correspondingly, the same g-factors, i.e., $g_1 \approx g_2 \approx 46$ (absolute value, 20% uncertainty). These g-factors are consistent with those obtained from tight-binding calculations (see the Supporting Information).

With regard to the orbital sub-band splitting, defined as $\Delta E = (E_{2,\uparrow} + E_{2,\downarrow})/2 - (E_{1,\uparrow} + E_{1,\downarrow})/2)$, we find that it decreases with V_G, going from $\Delta E = 12.5 \pm 3.5$ meV at $V_G = 2$ V to $\Delta E = 3 \pm 2$ meV at $V_G = 4$ V. This evolution is apparent from the relative V_C spacing between the barycenters of the first and second spin-split sub-bands, indicated by open circles and squares, respectively (each of these symbols is located halfway between the V_C positions of the ↑ and ↓ sub-band components).

Given the large g-factors, an even moderate B can induce crossings between sub-bands with opposite spin. For low V_G, where ΔE is maximal, the ↑ component of the second sub-band is expected to cross the ↓ component of the first sub-band for $B \approx 4.5$ T. As a result, at $B = 5$ T $E_{2,\uparrow}$ lies below $E_{1,\downarrow}$ for every V_G value. For relatively high V_G values, however, $E_{2,\uparrow}$ approaches $E_{1,\uparrow}$ closely due to the largely reduced ΔE, resulting in a virtual degeneracy and a first conductance step of $2e^2/h$ instead of e^2/h. Interestingly, this virtual degeneracy, occurring between parallel spin states, persists over a large V_G range, extending up to the largest value explored (5.8 V). From the discussion of Figure 2a, we conclude that tuning the potential landscape through V_G has a significant effect on the orbital sub-band splitting.

We now turn to the B-dependence of the 1D sub-bands. We investigate that for a fixed value of V_G. Figure 3a shows a map
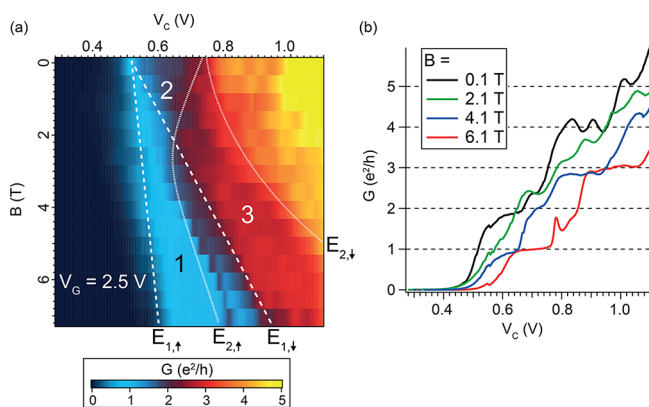
Figure 3. (a) Color plot of G(V_C,B) at $V_G = 2.5$ V. The dashed and dotted lines have the same meaning as in Figure 2b and were drawn after imposing the same g-factors as in that case and allowing for adjustable B-induced orbital shifts. A crossing between $E_{2,\uparrow}$ and $E_{1,\downarrow}$ occurs at ∼2 T. (b) The G(V_C) line cuts from the map in panel (a) at different fields. At $B = 6.1$ T (red curve), a dip of conductance can be observed in correspondence of the $2e^2/h$ plateau around $V_C = 0.8$ V.

of G as a function of V_C and B for $V_G = 2.5$ V. In the limit of vanishing B, G exhibits distinguishable plateaus at $2e^2/h$ and $4e^2/h$, consistently with the expected 2-fold Kramers degeneracy of the first two sub-bands. This is clearly visible in a G(V_C) line-cut at $B = 0.1$ T as shown in Figure 3b (here, the small applied B is necessary to suppress superconductivity in the Al-based contacts). Noteworthy, the plateaus are not as sharply quantized as at high B. The superimposed conductance modulation is due to a stronger backscattering at $B = 0.1$ T.

Increasing B results in a rapid splitting of the sub-band spin degeneracies. Using the same notation as in Figure 2b, the

onset of conduction through the different spin-resolved sub-bands has been indicated by dashed and dotted lines. To draw such lines, we have allowed for adjustable B-induced orbital shifts, and we have assumed B-independent g-factors equal to those measured at $B = 5$ T. This constrain was imposed to ensure consistency with the data of Figure 2b and to enable drawing lines also where the conductance steps are not clearly visible, such as the one associated with $E_{2,\uparrow}$ in the field range of $B < 4$ T.

The drawn lines follow fairly well the B-evolution of the spin-resolved conductance steps. According to our analysis, the sub-band edges $E_{2,\uparrow}$ and $E_{1,\downarrow}$ cross each other at $B \approx 2$ T. Around this B, however, the conductance plateaus cannot be discriminated, as apparent also from the G(V_C) trace at $B = 2.1$ T in Figure 3b. This crossing between $E_{2,\uparrow}$ and $E_{1,\downarrow}$ implies that at higher B, where conductance quantization emerges again, the ↑-spin channel of the second sub-band opens up before the ↓-spin channel of the first one. As a result, the three plateaus at e^2/h, $2e^2/h$, and $3e^2/h$, clearly visible in the 4.1 T G(V_C) trace in 3b or in the red trace of Figure 2a (at $B = 5$ T), correspond to the onset of conduction through the ↑-spin channel of the first sub-band, the ↑-spin channel of the second sub-band, and the ↓-spin channel of the first sub-band, respectively.

For $B > 6$ T, a pronounced conductance suppression develops in correspondence of the second plateau. Phenomenologically, this behavior resembles very much the one recently[28] observed by Kammhuber et al. and interpreted as a signature of a so-called "helical gap", namely an energy interval with an effectively spinless 1D mode.[3] When the electrochemical potential lies within this gap, G is supposed to drop from $2e^2/h$ to e^2/h, due to the lifted spin degeneracy. In combination with induced superconductivity, this spinless condition is essential to the development of Majorana-fermion states. Therefore, the direct experimental observation of helical 1D modes represents an important milestone in the field of topological superconductivity and Majorana fermions. From the V_C extension of the conductance dip, approximately 110 mV, we would deduce an energy gap of $E_b \approx 5.5$ meV. This value is comparable to the one found by Kammhuber et al. However, it exceeds by 2 orders of magnitude the spin−orbit energy given by tight binding calculations (see the Supporting Information), and the one measured in InSb nanowire quantum dots.[29] Here, however, by exploiting the tunability offered by the multiple gate geometry of our device, we show that the observed feature has in fact a different nature.

Figure 4a shows a G(V_C,$V_{G'}$) plot similar to the one of Figure 2a, where $V_{G'}$ has replaced V_G to parametrize the simultaneous sweeping of V_L and V_R along the white dashed line in Figure 1b, slightly shifted from the previous sweeping line (precisely: $V_L = V_{G'}$ and $V_R = \alpha_{R/L}(V_L - V_{L0})$, with $V_{L0} = 0$ and $\alpha_{R/L} = 0.875$). This plot is a collage of multiple measurements all taken at $B = 7.8$ T. A G(V_C) line cut at $V_{G'} = 2.87$ V, corresponding to values of V_L and V_R close to those of Figure 3, is shown in Figure 4b. In correspondence of the $2e^2/h$ plateau, we find the conductance suppression observed in the 6.1 T trace of Figure 3b. By analyzing its evolution as a function of $V_{G'}$, we can make some important observations. Upon decreasing $V_{G'}$, the conductance dip widens and deepens down to e^2/h. On its right side, the dip is followed by a well-defined $2e^2/h$ plateau. On its left side, however, the conductance approaches $2e^2/h$ for large $V_{G'}$, but it progressively decreases with $V_{G'}$, acquiring a sharp peak structure, which is characteristic of a tunnel
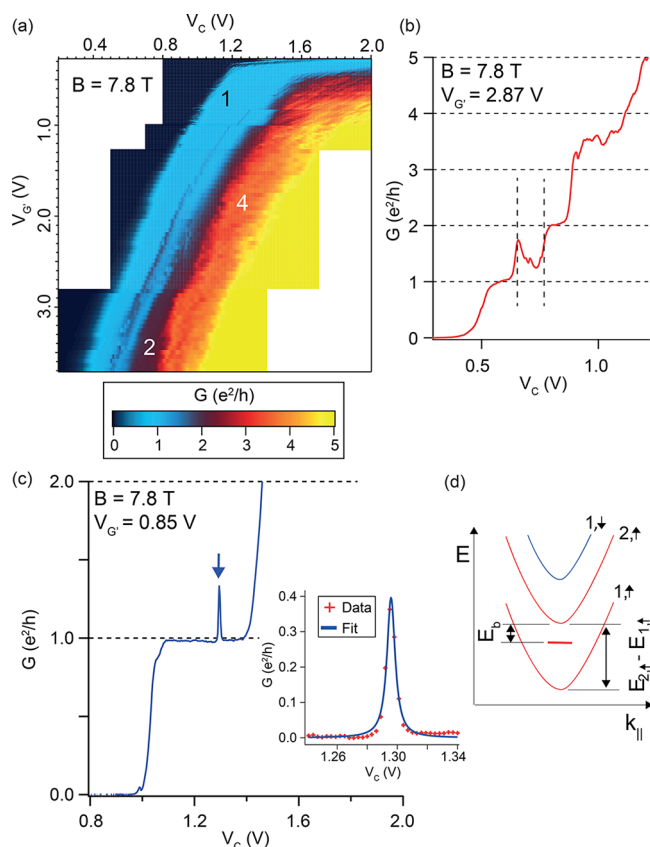
Figure 4. (a) $G(V_C, V_{G'})$ maps at B = 7.8 T; $V_{G'}$ parametrizes a sweep in (V_L, V_R) along the dashed line of Figure 1b. A sharp resonance on top of the e^2/h plateau, related to the second spin-polarized sub-band, evolves into a broad peak when $V_{G'}$ is raised. (b) Line cut from panel a at $V_{G'}$ = 2.87 V when the resonance is wide. The two vertical dashed lines indicate the energy extension ($E_b \approx 5.5$ meV) of the dip of conductance just after the resonance. (c) Line cut from (a) at $V_{G'}$ = 0.85 V, when the resonance (blue arrow) becomes sharp. Inset: Lorentzian fit of the resonance after removal of the background conductance. (d) Schematic band diagram showing the localized state with binding energy E_b relative to the second spin-up sub-band.

resonance through a discrete state, as shown in the line cut at $V_{G'}$ = 0.85 V in Figure 4c.

The inset of Figure 4c shows a Lorentzian fit of this peak after subtraction of the e^2/h background. The resonance width corresponds to an energy broadening $\Gamma = 0.29 \pm 0.05$ meV. This value largely exceeds the one expected from the temperature-induced smearing of the Fermi distribution function (i.e., 3.5 $k_B T = 0.08$ meV, where k_B is the Boltzmann constant). Therefore, Γ is dominated by the lifetime broadening of the discrete state due to tunnel coupling with the leads. The peak width increases with $V_{G'}$, while its position follows the $2e^2/h$ plateau keeping a constant spacing from the corresponding conductance step.

From the line shape of the conductance peak, we conclude that it arises from resonant tunneling through a bound state originating from the second spin-polarized sub-band. This localized state appears to be largely decoupled from the first sub-band (fitting to a Fano-shape line yields an only marginally better result). The dip width is determined by the binding energy of the localized state relative to the second spin-split sub-band. This interpretation rules out the original hypothesis of a conductance dip associated with a helical gap. An additional line cut from the topmost region of Figure 4a (displayed in the Supporting Information) reveals the presence of a conductance peak also before the onset of the first conductance plateau at e^2/h. This implies that, depending on the electrostatic potential landscape, a localized state can also emerge from the first spin-polarized sub-band.

The absence of quantum mechanical coupling between the resonant bound state and the first spin-polarized sub-band in Figure 4 suggests that the corresponding wave functions are spatially separated. To investigate this possibility, we have performed tight-binding calculations with an in-plane magnetic field aligned as in the experiment. The simulations take also into account the effect of the electric fields arising from gate biasing and surface charges (see the Supporting Information for a detailed discussion of these simulations). Figure 5 shows results at magnetic field B = 8 T for a distribution of negative charges at the InSb−HfO$_2$ interface. The energy of the lowest energy sub-bands is plotted as a function of the longitudinal wave-vector $k_{\parallel}$. As observed in the experiment, the first two sub-bands have the same spin-up polarization (we used red for up spins and blue for down spins). The squared wave functions of these two sub-bands are shown in the insets. They are
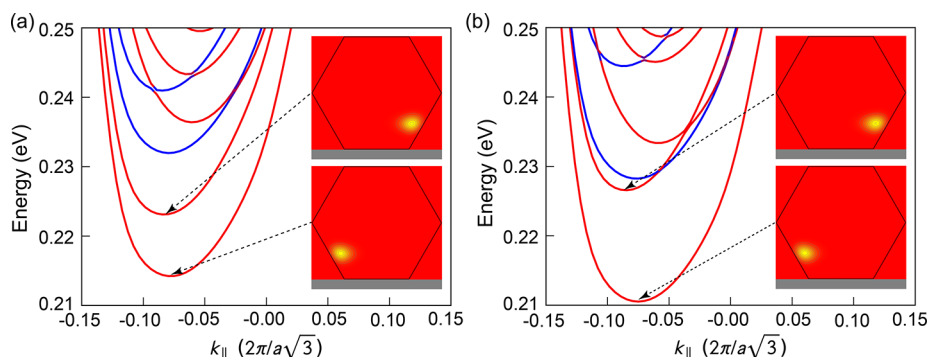
Figure 5. (a,b) Tight-binding band structure of an hexagonal InSb nanowire (diameter 160 nm) at magnetic field B = 8 T aligned as in the experiment. The calculation also accounts for the effect of gate-induced electric fields and surface charges (see the main text and the Supporting Information for details). $k_{\parallel}$ is the longitudinal wave vector, and a is the lattice parameter of InSb. The red (blue) curves correspond to spin-up (and spin-down) sub-bands. The squared wave functions of the lowest two sub-bands are plotted in the insets. They are strongly localized, extending over just ∼10 nm. The vertical confinement is due to the applied B, while the horizontal one is due to the in-plane electric field E_y from the gates and surface charges. The degeneracy between the left and right channels is lifted by a small $E_y = 0.1$ meV/nm in panel a and $E_y = 0.18$ meV/nm in panel b, yielding band structures approximately consistent with the experimental data of panels b and c of Figure 4, respectively.

strongly confined vertically by the magnetic field and laterally by the electric field from the surface charges. The first two sub-bands actually correspond to two side channels, which are split here by ~10 meV, comparable to the measured splitting. This splitting results from and is proportional to a small lateral electric field (~0.1 mV/nm), which we have deliberately introduced to account for a plausible slight asymmetry between the left and right of the nanowire (due, e.g., to an imbalance of surface charges or to the fact that the gates are not running perpendicular to the nanowire). These simulations show that electric and magnetic confinement can easily lead to the formation of distinct (uncoupled) channels in such nanowires, although the nature and localization of these channels is dependent on the specific distribution of charges around the nanowire. In such a scenario, the resonant feature in Figure 4 can be attributed to a defect or, more generically, a potential minimum localized near the wave functions of sub-band 2 but far from the wave functions of sub-band 1.

In conclusion, we presented conductance measurements reflecting the 1D band structure of an InSb nanowire under an in-plane magnetic field. By varying the potential landscape through the use of three bottom gates, we demonstrated large tunability of the intersub-band orbital spacing and, in particular, the unexpected possibility of robust, ground-state level degeneracies emerging at large B. These findings bare relevance to the study of topological phases in 1D superconductor—semiconductor structures. The occurrence of such exotic phases is in fact subordinated to special requirements on the 1D sub-band structure and filling condition. Finally, we also showed that discrete bound states can produce conductance resonances preceding the conductance plateaus. Whether such resonant bound states could account for the reported signatures of helical gaps in ref 25 is unclear, and we believe this possibility should deserve further investigation. The B-induced transverse localization discussed in the present work is expected to be a prominent effect in experiments where B exceeds ~1 T. At this field, the transverse localization, set by the magnetic length (~25 nm), becomes smaller than the typical nanowire radius.

■ ASSOCIATED CONTENT

Ⓢ Supporting Information

The Supporting Information is available free of charge on the ACS Publications website at DOI: 10.1021/acs.nano-lett.7b03854.

> The method for extracting the lever-arm parameters, g-factors, and sub-band splittings; measurements of an additional resonance before the first conductance plateau; calculations of the sub-band structure of the nanowire under external magnetic and electric fields; effect of an electric field along x, and experimental discussion. A table showing estimated lever-arm parameters. Figures showing differential conductance, details of Figure 4a, band structure, and wave functions. (PDF)

■ AUTHOR INFORMATION

Corresponding Author
*E-mail: silvano.defranceschi@cea.fr.

ORCID Ⓞ
Juan Carlos Estrada Saldaña: 0000-0003-4957-3742
Yann-Michel Niquet: 0000-0002-1846-1396
Diana Car: 0000-0002-6371-8285
Erik P. A. M. Bakkers: 0000-0002-8264-6862

Present Addresses
▽Center for Quantum Devices, Niels Bohr Institute, University of Copenhagen, 2100 Copenhagen, Denmark
○Condensed Matter Physics Center (IFIMAC), Universidad Autónoma de Madrid, 28049 Madrid, Spain

Notes
The authors declare no competing financial interest.

■ ACKNOWLEDGMENTS

■ REFERENCES

(1) Stanescu, T. D.; Tewari, S. Majorana fermions in semiconductor nanowires: fundamentals, modeling, and experiment. *J. Phys.: Condens. Matter* **2013**, *25*, 233201.

(2) Lutchyn, R.; Bakkers, E.; Kouwenhoven, L.; Krogstrup, P.; Marcus, C.; Oreg, Y. Realizing Majorana zero modes in super-conductor-semiconductor heterostructures. 2017, *arXiv:1707.04899*. arXiv.org e-Print archive. https://arxiv.org/abs/1707.04899, accessed on 2/20/2018.

(3) Oreg, Y.; Refael, G.; Von Oppen, F. Helical liquids and Majorana bound states in quantum wires. *Phys. Rev. Lett.* **2010**, *105*, 1−4.

(4) Lutchyn, R. M.; Sau, J. D.; Sarma, S. D. Majorana fermions and a topological phase transition in semiconductor-superconductor hetero-structures. *Phys. Rev. Lett.* **2010**, *105*, 077001.

(5) Brouwer, P. W.; Duckheim, M.; Romito, A.; von Oppen, F. Probability Distribution of Majorana End-State Energies in Disordered Wires. *Phys. Rev. Lett.* **2011**, *107*.10.1103/PhysRevLett.107.196804

(6) Lobos, A. M.; Lutchyn, R. M.; Sarma, S. D. Interplay of disorder and interaction in Majorana quantum wires. *Phys. Rev. Lett.* **2012**, *109*, 146403.

(7) DeGottardi, W.; Sen, D.; Vishveshwara, S. Majorana fermions in superconducting 1D systems having periodic, quasiperiodic, and disordered potentials. *Phys. Rev. Lett.* **2013**, *110*, 146404.

(8) Van Wees, B.; Van Houten, H.; Beenakker, C.; Williamson, J. G.; Kouwenhoven, L.; Van der Marel, D.; Foxon, C. Quantized conductance of point contacts in a two-dimensional electron gas. *Phys. Rev. Lett.* **1988**, *60*, 848.

(9) Li, Y.; Qian, F.; Xiang, J.; Lieber, C. M. Nanowire electronic and optoelectronic devices. *Mater. Today* **2006**, *9*, 18−27.

(10) Voisin, B.; Nguyen, V.-H.; Renard, J.; Jehl, X.; Barraud, S.; Triozon, F.; Vinet, M.; Duchemin, I.; Niquet, Y.-M.; De Franceschi, S.; Sanquer, M. Few-electron edge-state quantum dots in a silicon nanowire field-effect transistor. *Nano Lett.* **2014**, *14*, 2094−2098.

(11) Schroer, M.; Petta, J. Correlating the nanostructure and electronic properties of InAs nanowires. *Nano Lett.* **2010**, *10*, 1618−1622.

(12) Wallentin, J.; Ek, M.; Wallenberg, L. R.; Samuelson, L.; Borgstrom, M. T. Electron trapping in InP nanowire FETs with stacking faults. *Nano Lett.* **2012**, *12*, 151−155.

(13) Salfi, J.; Paradiso, N.; Roddaro, S.; Heun, S.; Nair, S. V.; Savelyev, I. G.; Blumin, M.; Beltram, F.; Ruda, H. E. Probing the gate-voltage-dependent surface potential of individual InAs nanowires using random telegraph signals. *ACS Nano* **2011**, *5*, 2191−2199.

(14) Holloway, G. W.; Song, Y.; Haapamaki, C. M.; LaPierre, R. R.; Baugh, J. Trapped charge dynamics in InAs nanowires. *J. Appl. Phys.* **2013**, *113*, 024511.

(15) Weis, K.; Wirths, S.; Winden, A.; Sladek, K.; Hardtdegen, H.; Lüth, H.; Grützmacher, D.; SchäPers, T. Quantum dots in InAs nanowires induced by surface potential fluctuations. *Nanotechnology* **2014**, *25*, 135203.

(16) Lu, W.; Xiang, J.; Timko, B. P.; Wu, Y.; Lieber, C. M. One-dimensional hole gas in germanium/silicon nanowire heterostructures. *Proc. Natl. Acad. Sci. U. S. A.* **2005**, *102*, 10046−10051.

(17) Ford, A. C.; Kumar, S. B.; Kapadia, R.; Guo, J.; Javey, A. Observation of degenerate one-dimensional sub-bands in cylindrical InAs nanowires. *Nano Lett.* **2012**, *12*, 1340−1343.

(18) Abay, S.; Persson, D.; Nilsson, H.; Xu, H.; Fogelström, M.; Shumeiko, V.; Delsing, P. Quantized conductance and its correlation to the supercurrent in a nanowire connected to superconductors. *Nano Lett.* **2013**, *13*, 3614−3617.

(19) Vigneau, F.; Prudkovkiy, V.; Duchemin, I.; Escoffier, W.; Caroff, P.; Niquet, Y.-M.; Leturcq, R.; Goiran, M.; Raquet, B. Magnetotransport subband spectroscopy in InAs nanowires. *Phys. Rev. Lett.* **2014**, *112*, 076801.

(20) Heedt, S.; Prost, W.; Schubert, J.; Grützmacher, D.; SchäPers, T. Ballistic transport and exchange interaction in InAs nanowire quantum point contacts. *Nano Lett.* **2016**, *16*, 3116−3123.

(21) Heedt, S.; Ziani, N. T.; Crépin, F.; Prost, W.; Schubert, J.; Grützmacher, D.; Trauzettel, B.; Schäpers, T.; Trellenkamp, St. Signatures of interaction-induced helical gaps in nanowire quantum point contacts. *Nat. Phys.* **2017**, *13*, 563.

(22) Gooth, J.; Schaller, V.; Wirths, S.; Schmid, H.; Borg, M.; Bologna, N.; Karg, S.; Riel, H. Ballistic one-dimensional transport in InAs nanowires monolithically integrated on silicon. *Appl. Phys. Lett.* **2017**, *110*, 083105.

(23) Gooth, J.; Borg, M.; Schmid, H.; Schaller, V.; Wirths, S.; Moselund, K.; Luisier, M.; Karg, S.; Riel, H. Ballistic one-dimensional InAs nanowire cross-junction interconnects. *Nano Lett.* **2017**, *17*, 2596−2602.

(24) van Weperen, I.; Plissard, S. R.; Bakkers, E. P. A. M.; Frolov, S. M.; Kouwenhoven, L. P. Quantized Conductance in an InSb Nanowire. *Nano Lett.* **2013**, *13*, 387−391.

(25) Kammhuber, J.; Cassidy, M. C.; Zhang, H.; Gül, Ö.; Pei, F.; de Moor, M. W. A.; Nijholt, B.; Watanabe, K.; Taniguchi, T.; Car, D.; Plissard, S. R.; Bakkers, E. P. A. M.; Kouwenhoven, L. P. Conductance Quantization at Zero Magnetic Field in InSb Nanowires. *Nano Lett.* **2016**, *16*, 3482.

(26) Gül, Ö.; Zhang, H.; Bommer, J. D.; de Moor, M. W.; Car, D.; Plissard, S. R.; Bakkers, E. P.; Geresdi, A.; Watanabe, K.; Taniguchi, T.; Kouwenhoven, L. P. Ballistic Majorana nanowire devices. *Nat. Nanotechnol.* **2018**, DOI: 10.1038/s41565-017-0032-8.

(27) Fadaly, E. M. T.; Zhang, H.; Conesa-Boj, S.; Car, D.; Gül, Ö.; Plissard, S. R.; Op het Veld, R. L. M.; Kölling, S.; Kouwenhoven, L. P.; Bakkers, E. P. A. M. Observation of Conductance Quantization in InSb Nanowire Networks. *Nano Lett.* **2017**, *17*, 6511−6515.

(28) Kammhuber, J.; Cassidy, M.; Pei, F.; Nowak, M. P.; Vuik, A.; Gül, Ö.; Car, D.; Plissard, S.; Bakkers, E.; Wimmer, M.; Kouwenhoven, L. P. Conductance through a helical state in an Indium antimonide nanowire. *Nat. Commun.* **2017**, *8*, 478.

(29) Nadj-Perge, S.; Pribiag, V.; Van den Berg, J.; Zuo, K.; Plissard, S.; Bakkers, E.; Frolov, S.; Kouwenhoven, L. Spectroscopy of spin-orbit quantum bits in indium antimonide nanowires. *Phys. Rev. Lett.* **2012**, *108*, 166801.